Acta Materialia 276 (2024) 120136

Contents lists available at ScienceDirect

Acta Materialia

journal homepage: www.elsevier.com/locate/actamat

Full length article

Atomistically informed mesoscale modelling of deformation behavior of bulk metallic glasses

Yuchi Wang [a], Yuchu Wang [b], Chaoyi Liu [b], Jinwoo Hwang [a], Yue Fan [b], Yunzhi Wang [a,*]

[a] Department of Materials Science and Engineering, The Ohio State University, Columbus, OH 43210, USA
[b] Department of Mechanical Engineering, University of Michigan, Ann Arbor, MI 48109, USA

ARTICLE INFO

Keywords:
Metallic glasses
Shear transformation
Activation energy
Shear-induced softening
Strength
Ductility

ABSTRACT

Both atomistic and mesoscale simulation techniques have been extensively employed to gain fundamental understanding of the structures, deformation mechanisms, and structure-property relationships in bulk metallic glasses (BMGs), each with its unique strengths and limitations. Nevertheless, there is a limited degree of synergistic integration between the two approaches. In this study, we extract key properties of shear transformation zones (STZs) directly from the atomistic simulations, including their size, number of shear modes, eigenstrain, and most importantly, the activation energy barrier spectrum as a function of cooling history and strain rate. We then incorporate these STZ properties into a heterogeneously randomized STZ dynamic model implemented in a kinetic Monte Carlo algorithm to study parametrically the deformation microstructure, shear band formation and stress-strain behavior of BMGs. Two important characteristics of STZ activation that dictate the strength and ductility of a glass are identified. One is the average of the activation energy barrier spectrum (approximated by a Gaussian distribution), determined by the glass composition and processing history such as the cooling rate. The other is the amount of shift of the Gaussian distribution towards smaller activation energy barrier values during deformation, which is determined by the initial structural states and strain rate during deformation, and exhibits a saturation value. These findings have allowed us to gain important fundamental insights into the correlation between the degree of shear-induced softening and the general deformation behavior of BMGs, leading to a better understanding of the correlation between the processing history/loading condition and the mechanical behavior.

1. Introduction

Bulk metallic glasses (BMGs) exhibit distinct properties not found in their crystalline counterparts, including high yield strength, elevated elastic strain, low shear modulus, a high coefficient of restitution, low coefficient of friction, and enhanced resistance to wear and corrosion. However, their utility is constrained by a notable drawback – poor ductility resulting from localized deformation. Different from the well-defined structural defects, plastic strain carriers and deformation mechanisms in crystalline materials, the corresponding entities are much more difficulty to identify in amorphous materials. This has hindered the development of a robust structure-property relationship in BMGs, making it difficult to effectively improve their ductility through microstructure engineering. For example, experimental observations have indicated that even a minor alteration in glass composition can result in a significant shift in ductility [1–4]. Studies have also demonstrated a noteworthy change in local atomic structure, specifically medium-range ordering, and heterogeneity within these compositions, which likely influences the observed changes in ductility [2]. Nevertheless, the precise mechanism through which alterations in local atomic structures contribute to changes in ductility remains unclear.

In recent years, both atomistic and mesoscale simulation techniques have been employed extensively to enhance our fundamental understanding of the structure, deformation mechanisms, and structure-property relationships in BMGs [5–30], each with its unique strengths and limitations. The atomistic simulations have revealed detailed local atomistic configurations and the associated energetics and mechanical properties [5–22]. For example, geometrically unfavored motifs (GUMs), which are loosely packed in contrast to the most energetically and geometrically favorable icosahedra short-range order (SRO), have been identified and proposed to be the “soft spots” and fertile sites for shear transformations [10,11]. Furthermore, the atomistic simulations have provided energetic information, such as the potential energy landscape (PEL) that offers a convenient theoretical framework to

* Corresponding author.
E-mail address: wang.363@osu.edu (Y. Wang).

https://doi.org/10.1016/j.actamat.2024.120136
Received 16 January 2024; Received in revised form 23 June 2024; Accepted 24 June 2024
Available online 26 June 2024

understand some complex process such as aging and rejuvenation during shear deformation of glass materials [19,23], and molecular motion, interaction, and structure changes in supercooled liquids and during glass formation [24,25]. Most importantly, the activation energies of local structural excitations (LSEs) and their minimum energy pathways (MEPs) associated with local shear transformations have been obtained by using a combination of atomistic simulations and an advanced saddle point search algorithm - the activation relaxation technique (ART) [15–21,31–33]. ART is able to identify saddle points between the energy state of the initial structure and the connecting neighboring local energy minima [31–33] without invoking any guesses or presumptions. These studies have highlighted the PEL changes at different structural and mechanical heterogeneities (i.e. heterogenous shear modulus) as well as the LSE behavior change under different thermal and loading conditions and the corresponding activation energy distributions [15–17,21]. For example, an externally applied stain has been shown to tilt the MEPs and create a second peak at smaller values in the Gaussian-type distribution of the activation energy barrier in a Cu-Zr metallic glass [21].

Although atomistic simulations can provide valuable information about the structures and energetics of LSEs, they are limited by the time and length scales. For the time scale limitation, although typical MD simulations can only reach nano seconds (far below the realistic experimental time scale), such a limitation can, to some extent, be remedied by properly combining energy landscape sampling algorithms with the transition state theory (TST). For example, by combining the ART-retrieved activation barriers spectra with the TST in a self-consistent manner [34,35], one can capture the heat-release signals of DSC experiments at realistic timescales without invoking arbitrary fitting parameters. On the other hand, as for the length scale limitation, it is more difficult to be remedied by atomistic modeling alone. For example, the typical thickness of a shear band in BMGs is about 10–100 nm [7,8,36–39], meaning that to simulate the formation of realistic shear bands the simulation boxes must be set much bigger, which are beyond the reach of most atomistic simulations. Thus, linking the important findings from the atomistic simulations directly to the heterogenous deformation (e.g. shear banding) in BMGs and extrapolating the findings from the atomistic model to the experimental scale are still challenging.

On the other hand, mesoscale simulations based on the shear transformation zone (STZ) model can simulate the deformation behavior of BMGs with the formation of shear bands, reflecting the disordered nature of glass in both long-range elastic interaction and PEL, and obtain the stress/strain fields and strain-stress curves. Please note that the shear transformation (ST) model originally proposed by Argon [26] to characterize plastic deformation of BMGs as plastic flow carried by the rearrangement of nanoscale volumes consider thermally activated events. It is then substantiated by Falk and Langer [6] through MD simulations performed at zero K to study the athermal deformation behavior of BMGs, in which they used STZ instead of ST to distinguish the athermal nature of their shear events. Since STZ is now widely used to refer to shear transformation events in MGs, no matter it is thermally activated or not [40], and for the sake of uniformity, we will call the individual shear event in our study STZ even though it is thermally activated. Based on the STZ model, Bulatov and Argon [27] used a kinetic Monte Carlo (kMC) algorithm with a uniform event catalog for all elements to study the thermally activated deformation behavior of BMGs at finite temperatures. Despite the identical catalog, thermal fluctuations and elastic interactions introduce randomness, leading to shear band formation. To enhance the capacity of this model for handling complex geometries and varying loading conditions, Homer and Schuh [28] replaced the Green's function approach with finite element analysis (FEA). This modification expanded the range of possibilities within the event catalog. This enhanced model found success in three-dimensional simulations. Lin et al. [41,42] considered the effect of free volume creation and annihilation in their model, which was further refined by Wang et al. [22], who introduced heterogeneity in shear modulus informed by atomistic simulations. Zhao et al. [29] introduced "heterogeneously randomized" event catalogs, where each voxel is born different, which matches the disordered nature of BMG atomic structures. We have used this heterogeneously randomized STZ model with a kMC algorithm to study the structure-property relationship of BMGs considering the strain-induced softening behavior [4,22,29,30]. By assuming different parameters that characterize STZs, the structural and mechanical heterogeneities (such as medium-range ordering (MRO) [4, 30] and heterogeneous shear modulus [22]) can also be included in the mesoscale simulations. However, mesoscale simulations based on the STZ models suffer from their assumptions made about crucial STZ properties. For example, the number of shear modes in [29] was determined by carrying out numerous simulations with increasing number of shear modes till the simulation results become independent of the number of shear modes. Consequently, it becomes imperative to derive essential STZ characteristics from experimental characterizations and atomistic simulation studies. This information is crucial for informing mesoscale models, enabling accurate predictions of the deformation behavior in specific BMG systems.

In this work, we integrate synergistically the atomistic and mesoscale simulations, capitalizing on each other's strengths and compensate for their weaknesses. In order to take full advantages of the atomistic simulation results, we employ the heterogeneously randomized STZ model [29] that allows us to incorporate directly the maximum amount of STZ information extracted from the atomistic simulations. For example, the key parameters of STZs extracted directly from the atomistic simulations and incorporated in the mesoscale STZ simulations include STZ size, number of shear modes, eigenstrain, and most importantly, the activation energy barrier spectrum (AEBS) (approximated by a Gaussian distribution), which were not well known before and needed to be assumed in an empirical manner. This atomistically informed STZ model is then implemented in a kMC algorithm to study the deformation microstructure, shear band formation, and the stress-strain behavior of BMGs. Two important characteristics of STZ activation that impact the strength and ductility of a glass are identified: the average of the activation energy barrier (determined by composition and processing history such as cooling rate of the MGs) and the amount of shift of the AEBS during deformation, which represents the softening behavior and exhibits a saturation value. The simulation results offer important insights into the effects of cooling rate and strain rate on the softening and deformation behaviors of BMGs, which will be discussed in detailed below, and their effects predicted by the mesoscale simulations match well with the experimental observations [43–53]. We find that the average activation energy barrier is responsible for the yield strength, while the softening effect is responsible for the ductility. The slower is the cooling rate, the larger is the average activation energy barrier and the larger is the degree of softening, the higher is the yield strength and the lower is the ductility at a fixed strain rate. For a given cooling rate, the higher is the strain rate, the larger is the extent of softening, the higher is the yield strength and the lower is the ductility.

The rest of paper is organized as follows. The method of both atomistic simulations and mesoscale simulations are presented in Section 2, including the method of atomistic simulations, the key parameters of STZs obtained from the atomistic simulations, and the methods of STZ model with the key parameters used in mesoscale simulations. In Section 3, the results about the AEBS change as a function of local strain and our corresponding softening formulation, and how the different average values and the amount of shift of AEBS influence the deformation behavior and mechanical properties are presented. The effects of cooling rate and strain rate are discussed in Section 4. Finally, the main findings are summarized in Section 5.

2. Methods

2.1. Methods of atomistic simulations

The system investigated in this study is a Cu-Zr alloy. Atomistic simulations are carried out using the Large-scale Atomic/Molecular Massively Parallel Simulator (LAMMPS) code, applying a widely adopted interatomic potential developed by Sheng et al. [54], which is an EAM-type potential that has been calibrated with first-principle calculations and demonstrated its reliability in reproducing experimentally measured physical and mechanical properties (e.g. glass transition point, structural factor, elastic moduli, etc.) [15,16,18–21,55–58]. The atomistic simulation box consists of 10,000 atoms with the composition of $Cu_{56}Zr_{44}$, which was prepared by quenching down an equilibrated high-temperature metallic liquid at the cooling rate of 10^{10} K/s. Then global shear strains (from 0 to 15 %) are applied to the sample at the conditions of 300 K and constant strain rate of 10^7 s^{-1}. Snapshots are extracted at intermediate strains, which have been further rendered to energy minimization before applying the Activation-Relaxation Technique (ART) to probe their underlying energy landscape. The obtained overall activation energy barrier spectra are then partitioned into various windows according to the local von Mises shear strain magnitude calculated at atomic level. For a selected atom, its relative atomic displacement (with respect to its nearest neighboring atoms) from the initial reference state (zero global strain state) to the given global shear strain state is calculated and further converted an atomic deformation gradient tensor F. Then its local strain tensor is calculated using Green-Lagrangian method:

$$\boldsymbol{E} = \frac{\boldsymbol{F}^{\mathrm{T}}\boldsymbol{F} - \boldsymbol{I}}{2} \tag{1}$$

Then, the von Mises strain is calculated using the formula:

$$E_v = \sqrt{E_{xy}^2 + E_{xz}^2 + E_{yz}^2 + \frac{\left(E_{xx} - E_{yy}\right)^2 + \left(E_{xx} - E_{zz}\right)^2 + \left(E_{yy} - E_{zz}\right)^2}{6}} \tag{2}$$

2.2. Key parameters of STZs derived from atomistic simulations

Key parameters of STZs, including their size, number of shear modes, eigenstrain, and most importantly, the activation energy barrier spectrum (AEBS) as a function of local strain, could be directly extracted from atomistic simulation results. The number of shear transformation modes of STZs, denoted as M, reflects various potential transformation pathways of STZ activation, leading to distinct "variants" characterized by different SFTSs during deformation. It should be proportional to the density of possible weak planes in a STZ introduced in [59,60] to characterize the number of possible local structural rearrangements. According to Zhao et al. [29], the number of shear modes can serve as an indicator of local structural symmetry and exert an influence on the mechanical properties. In crystalline regions or domains featuring high local symmetry within MGs, the value of M tends to be small. Consequently, the system encounters frustration in identifying a preferred shear mode by the local stress, thereby delaying the formation of shear bands. Conversely, in a homogeneous amorphous structure, M can be considerably larger. Nonetheless, due to the inherent spatial heterogeneity of structures in MGs, perfect isotropy at the scale of STZ size remains unattainable, and M cannot become exceedingly large. According to the findings of the parametric study [29], setting M to a value of 20 proves sufficient, as further increases beyond this threshold do not yield significant deviations from the current model.

This count of shear modes can actually be calculated directly through atomistic simulations [20]. Employing the ART algorithm, one can gather distributions of maximum atomic displacements from local minima to adjacent saddle points within the PEL under various cooling rates. The fictive temperatures of the samples prepared under different cooling rates can be estimated. Furthermore, the average displacement, denoted as $\overline{d}$, exhibits an Arrhenius-type dependence on the fictive temperature T_{fic}, expressed as $\overline{d} \propto \exp\left(\frac{\varepsilon_d}{k_B T_{fic}}\right)$, where ε_d can be fitted as around 0.146 eV. Considering M different STZ modes, the density of local energy minima in the PEL can be described as:

$$\rho = 1 \Big/ \overline{d}^M = \exp\left(-\frac{M \cdot \varepsilon_d}{k_B T_{fic}}\right), \tag{3}$$

which is similar to the formulation of STZ density [6,61]. Consequently, the term $(M \cdot \varepsilon_d)$ corresponds to the STZ formation energy E_f, which approximately amounts to half of the average cohesive energy per atom [61,62]. This estimation places the STZ formation energy at approximately 2.41 eV. Then, the number of shear modes can be approximately calculated as $M \approx E_f/\varepsilon_d = 16.5$ [20], which are closely in line with the finding from the parametric mesoscale simulation study. For different shear modes, the distribution of the deformation events in the strain space is assumed to be isotropic in previous studies [29,30]. This assumption has been validated by atomistic simulations according to the displacement vectors of the ART-probed local structural excitations at different global strain conditions, which indicate the nature of randomized displacement fields of atoms involved in STZs. The detailed analysis is shown in the Appendix.

To confirm the size of STZs, atomistic simulations were conducted to assess the typical size of a cluster of atoms being activated to the saddle point on the PEL, revealing an approximate diameter of 5 Å [16]. Accounting for a complete STZ transformation, which encompasses the relaxation process from the saddle point to the subsequent local minimum within the PEL, the number of involved atoms increases by a factor of 3 [18]. Consequently, the STZ size is determined to be roughly 7 Å. Additionally, the representative atomic displacement during the activation process measures around 1 Å [20]. Consequently, the characteristic simple shear strain is estimated to be 0.14. The form of the eigenstrain used in the simulations will be described in Section 2.3.

The initial average activation energy barrier can also be determined. Based on extensive atomistic simulations examining the AEBS under various cooling rates, a correlation between the average activation energy barrier and cooling rate in the absence of any stress bias has been established [19]. The activation energy barrier increases as the cooling rate decreases. However, it is essential to acknowledge that the cooling rates employed in these atomistic simulations exceed significantly the actual experimental cooling rate, which typically ranges between 10^4 and 10^6 K/s [63]. Extrapolating the average activation energy barrier to correspond to a lower cooling rate, approximately 10^5 K/s, suggests a value of approximately 2 eV.

To create a wide range of diverse local strain environments to further examine, with sufficient statistics, the local strain effects on the expected activation barriers, we conduct a dynamical deformation simulation (shown in Fig. 1). Need to note that, the dynamical deformation in typical MD simulations at unrealistically high strain rate will essentially suppress the thermal activations and create a stress-driven athermal scenario. In other words, what can be accessed and probed in MD simulations are only a low-barrier subset of all possible excitations in general thermal plasticity regime. However, the activation energy barriers spectra obtained by ART are much broader than the scope of MD and represent the available thermal excitations in different local strain environments. This is because the ART method is defined to probe the thermal excitations by introducing random perturbations and sampling the energy landscape. The spectra obtained by ART include high-barrier excitations (not just only small-barrier events), and the whole spectra information of realistic thermal excitations (as well as their dependence on local strains) could be extracted and incorporated into the mesoscale simulations.

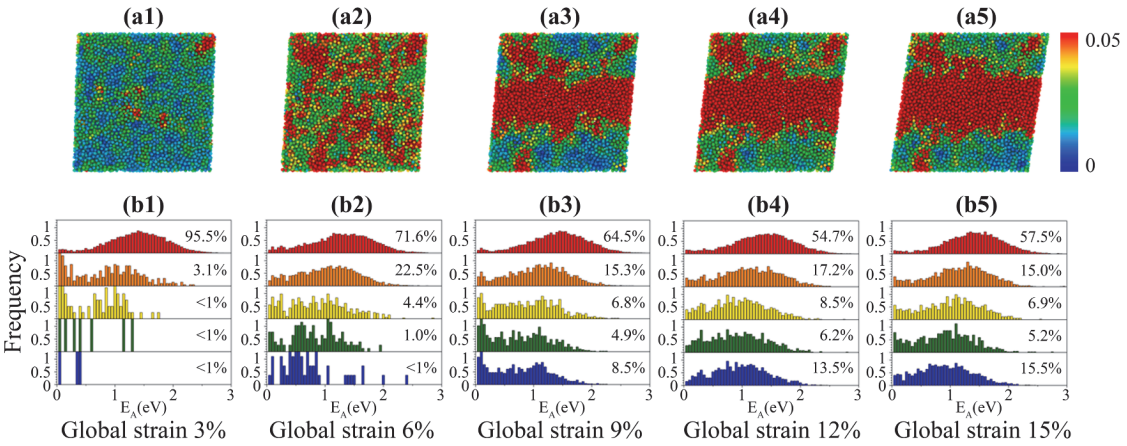

Fig. 1. The atomistically obtained (a) von Mises strain distributions at different global strains, and (b) the corresponding activation energy spectrum at different local von Mises strain. The windows with red, orange, yellow, green, and blue bars, represent the local von Mises strain <0.05, 0.05~0.1, 0.1~0.15, 0.15~0.2, and >0.2, respectively. The percentage numbers in each window represent the volume fractions of each strain region. (For interpretation of the references to color in this figure legend, the reader is referred to the web version of this article.).

2.3. Heterogeneously randomized STZ model of mesoscale simulations

In the current mesoscale simulations, we followed the method developed by Zhao et al. [29]. This model is based on the concept of shear transformation zone (STZ) proposed by Argon [26], which describes local atomic rearrangements that accommodate the shear deformation in BMGs. To describe the deformation process, we use generation g instead of time t, while $g = 0$ represents the initial configuration at $t = 0$. The generation change represents the STZ's atomic configuration change, transforming from one local minimum to another on the potential energy landscape (PEL) after activation. To reflect the disordered nature of glasses, each voxel (pixel in 2D) has a heterogeneously randomized event catalog, i.e., the STZ's shear modes, and the corresponding activation energy barriers and stress-free transformation strains (SFTS) (i.e., eigenstrains). Thus, different shear modes are characterized by a SFTS tensor, which can be expressed in 2D as:

$$\epsilon = \begin{bmatrix} \epsilon_1 & \epsilon_3 \\ \epsilon_3 & -\epsilon_1 \end{bmatrix} \tag{4}$$

It is assumed to be isotropic in both spatial and generation point of view and follow a Gaussian distribution. The value of ϵ_1 and ϵ_3 are extracted from standard Gaussian distribution and rescaled by the $\gamma_* /2$, with $\gamma_* = 0.14$ being characteristic simple shear strain value [29]. In the current study, a 2D computational supercell is devided into $N \times N$ pixels, with periodic boundary conditions applied along both dimensions. Each pixel is assumed to have M different shear transformation modes, so there are $M \times N \times N$ activation energy barrier values, $Q_i^{(m)}$, where $m = 1, 2, \cdots, M$ represents different transformation modes, and $i = 1, 2, \cdots, N \times N$ represents different elements (pixels). According to Eshelby [64], the plastic deformation is localized within the STZs, while the surrounding matrix responds elastically. This means that different STZs interact with each other via the elastic strain field. More detailed information about the elasticity calculations can be found in our previous work [29].

The simulations are carried out under uniaxial tension and a strain-controlled condition is applied. For each simulation step, a given strain rate $\dot{\varepsilon}$ and a strain increment $\Delta\varepsilon$ are imposed. If all the activation energy barriers $Q_i^{(m)}$ are positive, then the corresponding STZs need to be thermally activated. In this case, a kMC algorithm is used to determine the dynamics process.

The activation rate catalog consisting of $M \times N \times N$ transition states can be expressed as:

$$k_i^{(m)} = \nu_0 \exp\left(-\frac{Q_i^{(m)}}{k_B T} \right), \tag{5}$$

where ν_0 is the atomic vibration frequency related to the Debye frequency, k_B is the Boltzmann constant, and T is the absolute temperature. The average residence time can be calculated as [65]:

$$t_{res} = 1 \Big/ \sum_{i,m} k_i^{(m)}. \tag{6}$$

At the same time, for each simulation step during deformation, the probability of thermal plasticity in the time interval $\Delta t = \Delta\varepsilon/\dot{\varepsilon}$ can be described as $1 - \exp(-\Delta t/t_{res})$. A uniformly distributed random number $\eta \in (0, 1))$ is used to compare with the probability. If $\eta > \exp(-\Delta t/t_{res})$, the system will have thermal plasticity. A random number $\zeta \in (0, 1]$ is used to determine the transition state based on the kMC algorithm. The sum of the activation rate can be calculated as:

$$q_i = \sum_{j=1}^{i} k_j, \ i = 1, \cdots, M \times N \times N \tag{7}$$

where $k_j, j = 1, \cdots, M \times N \times N$, is the activation rate of different transition state expressed in Eq. (5). If the random number ζ satisfies $q_{s-1} < \frac{\zeta}{t_{res}} \le q_s$, then the transition state, s, is selected. On the other hand, if $\eta \le \exp(-\Delta t/t_{res})$, the system cannot be thermally activated during this time interval and it can only have pure elastic deformation. In addition to these two cases, if the atomic configuration of an STZ becomes unstable under large stresses, athermal plasticity will take place instantaneous.

To describe the activation energy barrier clearly, the softening behavior is also a critical effect we need to reflect in our simulations. The shear transformation strain induced softening phenomenon has been widely observed in BMGs [66,67]. Once a voxel in the initial structural state (generation 0) is transformed, it becomes generation 1 and has a new structural state (a perturbed structural state) surrounded by new activation energy barriers. Each time after a shear transformation, the activation energy barriers for the next shear event will be lowered. This softening is believed to be associated with local structure changes during the deformation process [7,68]. At the beginning, the atomic structure of a glass is well-relaxed (annealed) and stays at a low energy configuration. The atoms have to overcome a high barrier to reach the neighboring local minima. However, under an external load, the atoms in the STZ are forced to separate. The atoms have their new neighbors and the

original short-range order if any is disrupted, so the atoms are less geometrically compatible and, thus, at higher energy states. Therefore, the local atomic environment will be easier to activate (i.e., has a lower activation energy barrier) for the next generation of transformation.

By considering the softening effect and the work term, the actual activation energy barriers can be written as:

$$Q^{(m)} = \Delta F_* \exp\left(-\eta_g\right) - \frac{1}{2} V_g \sigma_{ij} \epsilon_{ij}^{(m)}, \tag{8}$$

where ΔF_* represents the activation energy barrier without external stress, which is equal to the Helmholtz free energy difference between the initial state and the saddle point, η_g is the amount of local softening at generation g, and the last term represents the work done by the local stress σ_{ij} during deformation, where V_g is the volume of STZ at generation g and $\epsilon_{ij}^{(m)}$ is the stress-free transformation strain (SFTS) tensor for shear transformation mode m. More details are discussed in Section 3.1.

2.4. Incorporating parameters from atomistic simulations into the STZ model

To parameterize the STZ model, we incorporate directly the key parameters of STZs, including their size, number of shear modes, eigenstrain, and the AEBS, as a function of local strain, extracted from the atomistic simulation results (as presented in Section 2.2), in our mesoscale simulations. These parameters are listed in Table 1. In addition, the 2D computational cell consists of 512 × 512 grid points in the mesoscale simulations, since each grid point represents a STZ and the average size of the STZ is ~0.7 nm according to the atomistic simulations [16,18], the physical size of the computational cell is 358.4 nm × 358.4 nm. For the parametric studies, we test three different average activation energy barriers 1.8, 2, and 2.2 eV, which corresponding to three different cooling rate ~ $10^{7.25}$, $10^{5.75}$, and $10^{4.25}$ K/S, according to the tendency obtained by the atomistic simulations [19].

3. Results

3.1. Shear-induced activation energy barrier spectrums change from atomistic simulations and formulation of softening in mesoscale modeling

The AEBS obtained for Cu-Zr MG using the ART method show significant differences between samples with and without an applied shear strain. More specifically, a new peak with low activation energy barriers emerges under an external load [21]. This finding seems to agree with previous studies [17,70,69], which show that the activation energy barrier of a deformed sample is smaller than that of an undeformed sample. To analyze how the AEBS changes as a function of local strain, more atomistic calculations are carried out. A sample is prepared with a total of 10,000 atoms. The sample size at 0 strain is 92.34 Å × 92.34 Å × 20 Å. Shear strains varying from 0 to 15 % are applied to the sample at a constant strain rate of 10^7 s^{-1} and a constant temperature of 300 K. The von Mises strain distributions at different global strains are shown in Fig. 1(a). Under the applied shear loading, a shear band is formed at the center of the system. To see how the AEBS changes as a function of local Von Mises strain, the AEBSs are divided into five windows within different local strain regions. As shown in Fig. 1(b), the average values of the activation energy barriers decrease as a function of local von Mises strain and saturate at high local strains. This indicates that those STZs located in the shear band possesses smaller activation energy barriers. The shifting of the peak of AEBS towards smaller values saturates when it reaches the upper limit, i.e., when the structure has arrived at a supercooled liquid state. During the loading process, the volume fraction of the high local strain regions increases as the global strain increases, so does the volume fraction of STZs with smaller activation energy barriers as shown in Fig. 1. That is the reason for the emergence of the peak with smaller activation energy barriers in the total spectrum under loading. The consequence of such a strain- or generation-dependent softening will be further discussed in Section 4.1.

Table 1
List of simulation parameters.

Parameter	Value
Young's modulus E	69.46 GPa [30]
Poisson's ratio ν	0.365 [30]
Average activation energy barrier ΔF_*	1.8 / 2 / 2.2 eV
Eigenstrain γ_*	0.14
STZ size l_0	0.7 nm
Number of shear modes M	20
Temperature T	300 K
Strain rate $\dot{\epsilon}$	10^{-4}~10^2 s^{-1}

Besides the local strain-induced activation energy barrier spectrums change during deformation, other factors can also influence the initial activation energy barrier and the subsequent shifting. Based on the results from the atomistic simulations, varying cooling rates employed during the glass preparation process results in different degree of relaxation and distinct initial energy states, and leads to different corresponding activation energy barriers [15,16,18,19,34,70,69,71]. As the cooling rate increases, the atomic structure of a glass becomes increasingly less stable (i.e., at higher and higher energy states) and accordingly the average activation energy barrier for STZ decreases [15–19,34,70,69,71]. Notably, at extremely high cooling rates, the structural state (energy level and activation energy barrier) asymptotically approaches to a limit determined by the supercooled liquid state and, thus, further reductions are no longer feasible. The high local strain region within the shear band bears resemblance to the behavior of supercooled liquid [12–14,72], with its activation energy barrier (and thus the yield stress) constrained by a comparable saturation threshold. Consequently, increasing cooling rates bring the activation energy barrier closer to this saturation value, reducing the degree for softening. In essence, increasing the cooling rate leads to a decline in the average activation energy barrier until it approaches this saturation point, concurrently diminishing the extent of softening.

In order to incorporate these new findings in mesoscale simulations and describe our activation energy barrier spectrums accordingly, we correlate the activation energy barrier spectrums change with the softening behavior. Following the findings in atomistic simulations, we can describe the PEL during the shear transformation process as the schematics illustrated in Fig. 2. This process can be used to reflect a decrease in the activation energy barrier as the local strain (generation) increases, and it also works for different initial activation energy barrier spectrums. As described in Section 2.3, the shear transformation strain induced softening phenomenon can be reflected in the STZ model by a generation dependent softening factor η_g that represents the amount of local softening at generation g. Here the formulation of η_g will be developed to introduce the findings in the atomistic simulations.

The recovery process during deformation needs to be considered in the softening behavior. In the study about the effect of temperature and strain rate by Dubach et al. [43], they collected the stress-strain curves and deformation behaviors of a Zr-based BMG at different temperature and strain rates. The results show that for a given temperature, when the strain rate is low, a non-uniform shear deformation characterized by serrated flow appears in the stress-strain curves, and when the strain rate is high, the flow behavior is uniform. This serrated flow is believed to be governed by a diffusional relaxation process, and this structural relaxation helps to make the local atomic configuration partially recovered. For each given temperature, there is a critical strain rate for the diffusional relaxation process to happen, and there is an Arrhenius-type dependence of the critical strain rate on temperature. According to the fitting to experimental data by the Arrhenius equation, an activation energy barrier, $Q^{act} = 0.37\ eV$, has been obtained for the activation of the diffusional relaxation process [43]. The characteristic time of the

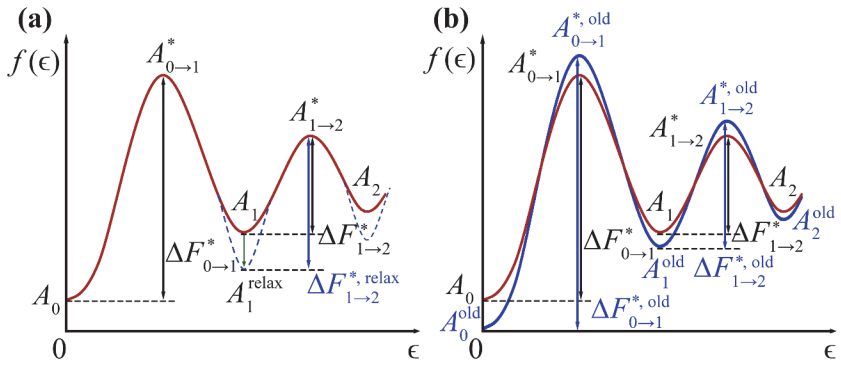

Fig. 2. The schematics of the energy landscape during the transformation process considering softening. (a) With partial recovery under diffusional relaxation process. (b) With different initial state by different preparation process.

relaxation process can be calculated as:

$$\tau = \frac{1}{\nu_0 \exp(-Q^{act}/k_B T)}, \tag{9}$$

where ν_0 represents the atomic vibration frequency. As shown schematically in Fig. 2(a), after such structural relaxation during a time span in between two shear transformation events under a given strain rate, the local energy state will be lowered and the activation energy barrier for the next shear transformation will be higher. This means that the shear transformation induced softening could be partially recovered by the structural relaxation. Such an impact on softening could be described by a temporary softening term related to the relaxation time. However, even though the local structure is fully relaxed, the system cannot reach the same energy as the initial state, so there is still a permanent softening part that cannot be recovered without thermal annealing and will be accumulated during repeated shear transformations [29]. By combining these two parts, we can describe the softening behavior as:

$$\eta_g = \eta_g^p + \eta^t \exp\left(-\frac{t_{elap}}{\tau}\right), \tag{10}$$

where η_g^p is the generation-dependent permanent softening and η^t is the maximum temporary softening. t_{elap} represents the time elapsed since the last shear transformation of a certain location. If the structure has little time to relax, such as loading at an extremely high strain rate, then t_{elap} will be much smaller than τ and the temporary softening term will be closer to η^t, leading to the maximum softening effect (i.e., the given location will have the lowest activation energy barrier to be activated in the next STZ event). In contrast, if the structure is well relaxed, then t_{elap} will be much larger than τ, and the temporary softening term will be closer to 0, leading to the smallest softening effect. If we treat the initial system as a well-annealed and homogeneous system, then $\eta_0 = 0$ for all the elements.

To address the softening term quantitatively, the values of the softening parameters η_g^p and η^t can be determined as functions of the local von Mises strain invariant ϵ^{Mises}:

$$\eta_{g+1}^p = \eta_g^p + \kappa_p \left(\epsilon^{Mises}\right)^2, \tag{11}$$

$$\eta^t = \kappa_t \left(\epsilon^{Mises}\right)^2, \tag{12}$$

where κ_p and κ_t are constants. In current study, we assume $\kappa_p = 13$ and $\kappa_t = 39$ to reach similar amount of shift as the atomistic simulations. So that the softening will be strain-dependent, i.e., the activation energy barrier will decrease as a function of the local strain.

There should be an upper limit for softening (and thus for η_g^p) when the local atomic configuration in the STZ volume under consideration asymptotically approaches to that of a supercooled liquid [12–14]. As shown in Fig. 2(b), different initial structures are expected for glasses with different preparation histories such as the cooling rate, which could lead to different initial activation energy barriers. Since the upper limit for softening is fixed, the maximum amount of softening η_{max} will also be different.

To illustrate the softening behavior in the form of activation energy barrier change, the schematic plots of the AEBSs (approximated by Gaussian distributions) before and after softening as a function of cooling rate and strain rate are shown in Fig.3. We consider two main factors: the average value of the Gaussian distribution, Q, which is determined by the cooling rate, and the shift of the Gaussian, ΔQ, which reflects the degree of softening. The width of the Gaussian is assumed to be the same for all cases according to the atomistic simulation results [19]. When the strain rate is extremely high, there is no time for relaxation during deformation and the softening effect is maximized (i.e., $\Delta Q \sim \Delta Q_{max}$) and the activation energy barrier could reach the saturation value, as indicated by the red dotted line shown in the right column of Fig.3. At the same strain rate, samples prepared at a faster cooling rate will have a higher energy state associated with their initial structure state and the activation energy barrier for shear transformation will be lower and thus closer to the saturation value. Therefore, the softening effect will also become weaker when the cooling rate during glass preparation is higher. Some mesoscale elastoplastic simulations also indicate that a more stable initial structure (i.e., having a larger activation energy barrier for STZ activation) leads to a larger stress drop (extent of softening) after yielding [73]. When the strain rate is relatively slow, the perturbed atomic configurations by the shear transformation will have time to relax, lowering its potential energy and increasing the activation energy barriers surrounding the potential energy well. In this case, the structural state could not approach to the supercooled liquid state (red dotted line in Fig. 3.), leading to a smaller room (i.e., lesser degree) for softening. This difference in ΔQ comes from

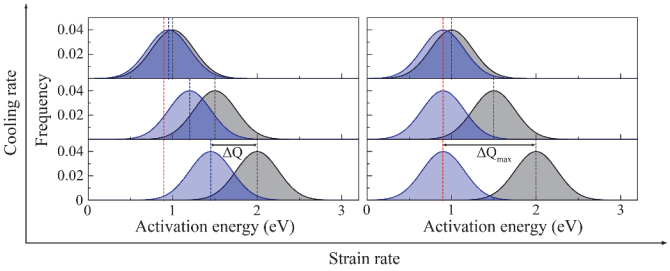

Fig. 3. Schematic plots of the activation energy barrier spectrums before (black) and after (blue) softening as a function of cooling rate and strain rate. The black and blue dash line show the average activation energy before and after the softening, and the red dash line shows the saturation value. (For interpretation of the references to color in this figure legend, the reader is referred to the web version of this article.).

the effect of temporary softening. More analysis and results about the effect of cooling rate and strain rate on deformation impacted by softening will be discussed in Section 4.

Incorporating the atomistic simulation findings into our mesoscale STZ dynamic modeling, as depicted in Figs. 2 and 3, has allowed us to study parametrically the deformation microstructure, shear band formation and stress-strain behavior of MGs. Parametric studies of the effects of Q and ΔQ will be presented in the following sections.

3.2. Effects of two main factors on the deformation behavior and mechanical properties of BMG

3.2.1. Effect of the average activation energy barrier

Three distinct average activation energy barriers, $Q1 = 1.8\ eV$, $Q2 = 2\ eV$, and $Q3 = 2.2\ eV$, have been employed to assess their impact on deformation, while maintaining an equivalent shift of the AEBS, $\frac{\Delta Q}{Q}$, a constant strain rate of $10^{-4}\ s^{-1}$ and a constant upper limit for the AEBS shift, $\eta_{max} = -\ln 0.6$. Consequently, we have $Q1 < Q2 < Q3$, with $\frac{\Delta Q1}{Q1} = \frac{\Delta Q2}{Q2} = \frac{\Delta Q3}{Q3} = 0.165$. These Q values are chosen by extrapolating the average activation energy barrier from the atomistic simulation results to the actual experimental cooling rate and the ΔQ values are chosen based on the amount of shift obtained by the atomistic simulations. As depicted in Fig. 4(a,c), a higher activation energy barrier leads to a higher yield strength. This trend can be attributed to the fact that, in accordance with Eq. (5), a greater activation energy barrier corresponds to a reduced activation rate. Consequently, it becomes more difficulty for STZs to activate, delaying yielding and boosting the yield strength. To investigate the change in ductility based on the deformation microstructure (illustrated in the von Mises strain maps) at a 2 % plastic strain as depicted in Fig. 4(b), we employ extreme site analysis [29,30] and the strain localization index [22]. In this study, voxels with accumulated local strain exceeding 0.7 are identified as extreme sites. Samples exhibiting fewer extreme sites are presumed to possess greater damage tolerance and enhanced ductility [29,30]. Additionally, concerning shear band propagation, a localized shear band makes the MG more brittle. To quantify the extent of strain localization, we compute the strain localization index, represented as the standard deviation of the local von Mises strain across all voxels for various cases. All the following extreme site analysis and the strain localization index are collected at 2 % plastic strain. These tests are replicated more than five times using different random seeds to obtain error bars. As shown in Fig. 4(d), both the count of extreme sites and the strain localization index exhibit similar values across all three cases. This suggests that all three glasses possess similar ductility characteristics even though they have drastically different yield strength. Thus, these findings highlight that the alterations in average activation energy barriers primarily impact the yield strength, with no discernible influence on ductility when the relative shift of AEBS remains consistent.

3.2.2. Effect of shift of the activation energy barrier spectrum

To investigate the impact of the AEBS shift, which reflects the softening effect elaborated upon in Section 4, we keep the average activation energy barrier constant (i.e., $Q1 = Q2 = Q3 = 2$ eV) while varying ΔQ. This gives rise to three distinct cases designated as softening1, softening2, and softening3, respectively, corresponding to $\eta_{max} = -\ln 0.8$, $\eta_{max} = -\ln 0.7$, and $\eta_{max} = -\ln 0.6$. These cases are characterized by $\frac{\Delta Q1}{Q1} = 0.085$, $\frac{\Delta Q2}{Q2} = 0.125$, and $\frac{\Delta Q3}{Q3} = 0.165$, all of which are subjected to an identical strain rate of $10^{-4}\ s^{-1}$. In contrast to the previous cases presented in Section 3.1, the yield strengths of these three glasses are almost the same. However, as the shift of the AEBS intensifies from softening-1 to softening-3, the stress-strain curves manifest larger stress drops, indicative of reduced ductility. Moreover, the deformation microstructure undergoes a profound transition from a uniform to a highly localized strain distribution, as shown in Fig. 5(b). The probability density distributions of von Mises strains across distinct voxels in the three cases, presented in Fig. 5(d) at a 2 % plastic strain, exhibit a common peak position attributable to the same eigenstrain. Nonetheless, a longer tail emerges in the distribution as the shift becomes more pronounced, signifying more substantial inelastic transformations. Furthermore, the extreme site occurrence and the strain localization index (Fig. 5(e)) increase significantly as the shift of the AEBS intensifies. This underscores that a greater shift in the AEBS, i.e., a greater degree of softening, corresponds to reduced ductility. These results highlight that the variations in the degree of softening during

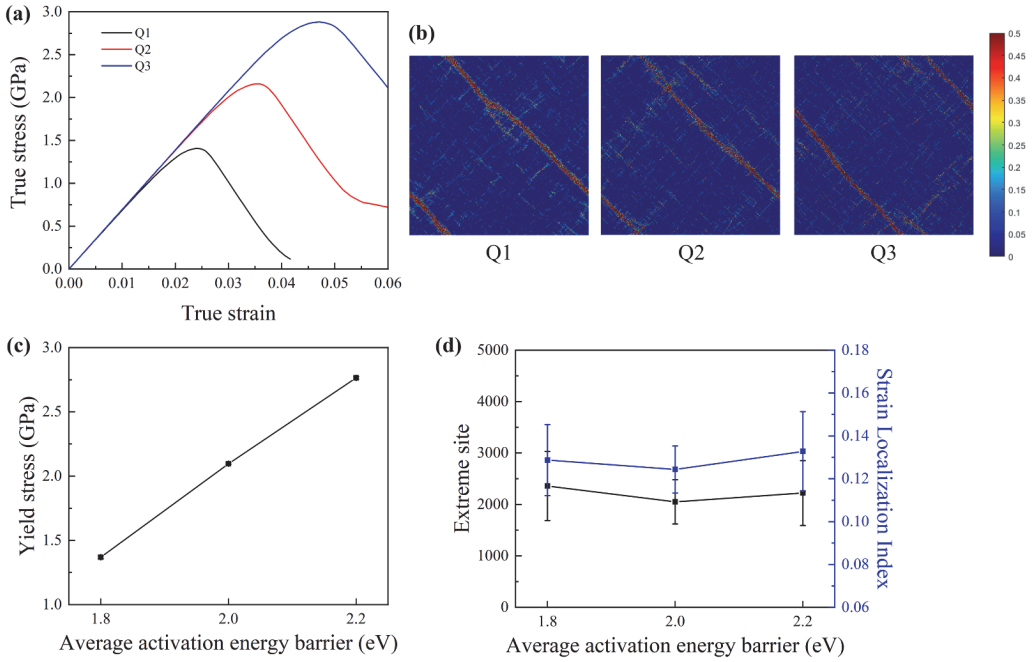

Fig. 4. Effect of average activation energy barriers. (a) Stress-strain curves, (b) the deformation microstructure (i.e., von Mises strain maps) at 2 % plastic strain, (c) yield stress, and (d) number of extreme sites and strain localization index, for three different average activation energy barriers, $Q1$=1.8 eV, $Q2$=2 eV, and $Q3$=2.2 eV.

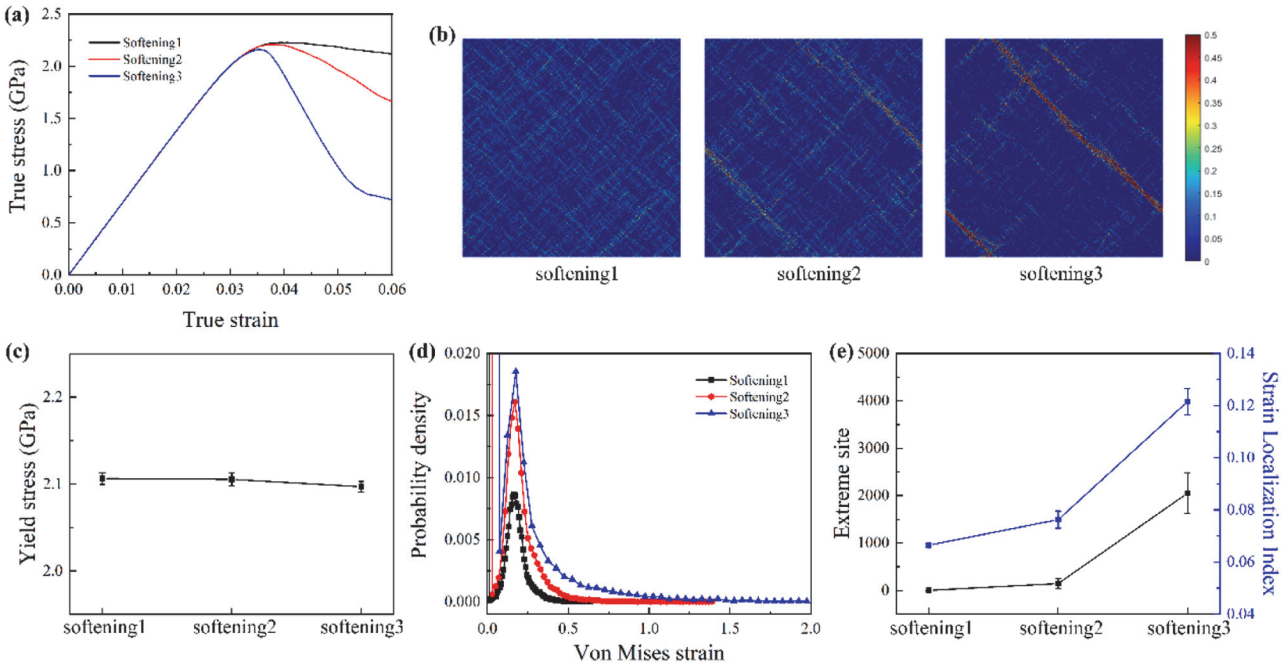

Fig. 5. Effect of softening. (a) Stress-strain curves, (b) the deformation microstructure (i.e., von Mises strain maps) at 2 % plastic strain, (c) yield stress, (d) the probability density distribution of the Von Mises strain, and (d) number of extreme sites and strain localization index, for three different softening behavior, $\eta_{max} = -\ln 0.8$, $\eta_{max} = -\ln 0.7$, and $\eta_{max} = -\ln 0.6$, named softening1, softening2, and softening3.

deformation primarily impact ductility while leaving yield strength unaffected.

4. Discussion

Combining the two tests presented in Section 3, we learned that the average of AEBS is responsible for the yield strength while the amount of its shift towards smaller average values during deformation (i.e., the softening behavior) is responsible for the ductility. With this finding, we could analyze the effects of cooling rate during glass preparation and strain rate during deformation on the deformation behavior and mechanical properties of BMG.

According to the experimental observations on the impacts of thermal history such as cooling rate during glass preparation [44–48] and strain rate during deformation [43,48–53] on the deformation behavior and mechanical properties of BMGs, the slower is the cooling rate, the higher is the yield strength and the lower is the ductility at a fixed strain rate [44]. For a given glass (i.e., given composition and cooling rate), the higher is the strain rate, the higher is the yield strength and the lower is the ductility [48,50–52]. Some analyses have been provided to explain these observations. For the effect of cooling rate, the local atomic configuration change after quenching can be considered as a structural defect that impacts the mechanical properties, and a slower cooling rate gives the atoms more time to reach their local ordered equilibrium positions. Thus, a slower cooling rate would lead to a more ordered atomic structure [44–46]. For the effect of strain rate, the shear band emission and propagation are considered as a recovery process that is quite different with different strain rate. When the strain rate is low, many shear bands are formed discretely and the deformation is more homogeneous. The yield strength will be low because the shear bands release the strain early, but the ductility will be high due to the sufficient time for the recovery process. When the strain rate is high, the shear bands do not have sufficient time to propagate and recovery. The stress increases rapidly to a high level, and then form a highly localized shear band that leads to poor ductility [51]. These analyses offer some insights into the impacts of cooling rate and strain rate on deformation at the intuitive level, but the quantitative relationships among the structural and energetic properties of STZs, the softening behavior during deformation, the deformation microstructure and the mechanical properties are yet to be illustrated.

4.1. Effect of cooling rate on the deformation behavior and mechanical properties

The findings from atomistic simulation and experimental studies could be captured by the two key parameters characterizing AEBS in our mesoscale STZ dynamic model, i.e., variation in the average activation energy barrier and the extent of AEBS shift during deformation. Based on atomistic simulations examining the AEBS under various cooling rates, we learned that the activation energy barrier increases as the cooling rate decreases, and they are further away from the saturation threshold [19]. Extrapolating from the atomistic simulation results to the actual experimental cooling rate, we set $Q1 = 1.8\ eV$, $Q2 = 2\ eV$, and $Q3 = 2.2\ eV$, correlating with decreasing cooling rates, and η_{max} values of $-\ln 0.67$, $-\ln 0.6$, and $-\ln 0.55$, respectively. Consequently, they yield $\frac{\Delta Q1}{Q1} = 0.139$, $\frac{\Delta Q2}{Q2} = 0.165$, and $\frac{\Delta Q3}{Q3} = 0.218$. All three cases are subjected to an identical strain rate of $10^{-4}\ s^{-1}$, yielding $Q1 < Q2 < Q3$, and $\frac{\Delta Q1}{Q1} < \frac{\Delta Q2}{Q2} < \frac{\Delta Q3}{Q3}$. Since the correlation between cooling rate and activation energy barrier spectrum has been established [19], we can capture the cooling rate effect following the same tendency of the activation energy barrier change. As depicted in Fig. 6, as the cooling rate decreases, the yield strength increases while the ductility decreases. Samples subjected to lower cooling rates exhibit more localized shear bands (Fig. 6(b)) and significantly higher counts of extreme sites and strain localization indices (Fig. 6(d)). During deformation, the larger amount of activation energy barrier decrease facilitates the local STZ to deform again, this autocatalytic effect defined by the softening leads to strain localization. Combining the effects outlined in Section 3, we can conclude that a reduced cooling rate results in a higher average activation energy barrier, contributing to a greater yield strength. Simultaneously, it leads to a more substantial shift of the AEBS and heightened softening effects, and consequently reduced ductility.

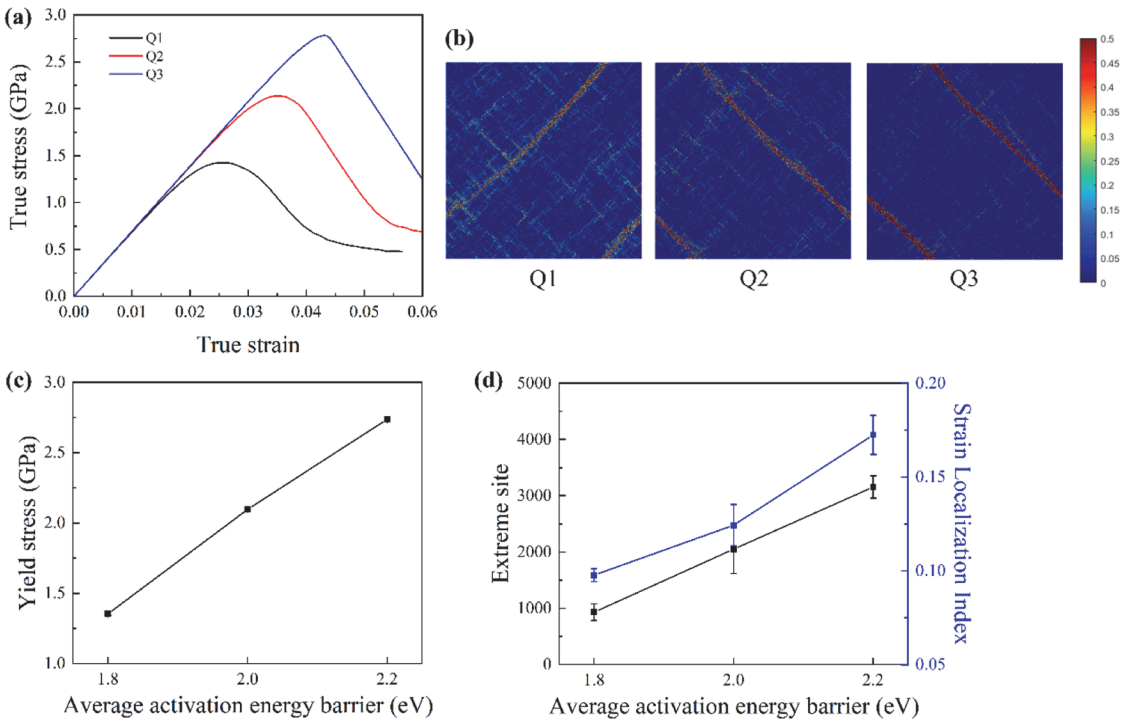

Fig. 6. Effect of cooling rate. (a) Stress-strain curves, (b) the deformation microstructure (i.e., von Mises strain maps) at 2 % plastic strain, (c) yield stress, and (d) number of extreme sites and strain localization index, for three different cooling rates with $Q1 < Q2 < Q3$, and $\frac{\Delta Q1}{Q1} < \frac{\Delta Q2}{Q2} < \frac{\Delta Q3}{Q3}$.

4.2. Effect of strain rate on the deformation behavior and mechanical properties

While the degree of structural relaxation and initial PEL of a BMG are determined by its preparation process, diffusional relaxation during deformation has the potential to alter the energy state and activation energy barrier, as depicted in Fig. 2(a). The local structural relaxation occurring after an STZ event results in reduced energy levels at the local minimum and an elevated activation energy barrier for subsequent transformations [7,29,51]. The extent of relaxation and the magnitude of energy reduction are contingent upon the strain rate and are determined by the temporary softening detailed in Section 3.1.

To investigate the influence of strain rate on the deformation behavior and mechanical properties of BMGs, we use seven different strain rates, ranging from 10^{-4} s^{-1} to 10^{2} s^{-1}. All the seven cases maintain a consistent average activation energy barrier (2 eV) and share an

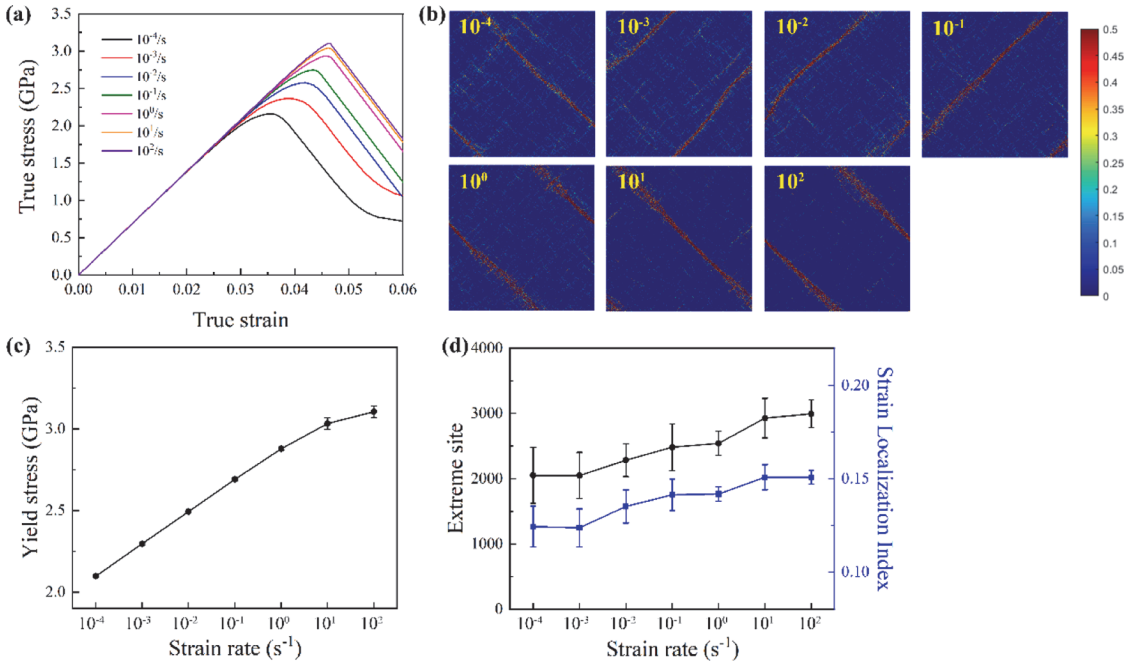

Fig. 7. Effect of strain rate. (a) Stress-strain curves, (b) the deformation microstructure (i.e., von Mises strain maps) at 2 % plastic strain, (c) yield stress, and (d) number of extreme sites and strain localization index, for seven different strain rates.

identical upper limit for permanent softening ($\eta_{max} = -\ln 0.6$). As the strain rate escalates, the shift in the AEBS, reflecting the extent of softening, increases. Specifically, we apply $\frac{\Delta Q}{Q} = 0.165$ for the strain rate of 10^{-4} s^{-1}, same as the value we used in previous tests, and $\frac{\Delta Q}{Q} = 0.215$ for the strain rate of 10^{2} s^{-1} calculated by the Eqs. (8) and (10), while all other parameters are fixed. As illustrated in Fig. 7(a,c), the yield strength rises with increasing strain rate. A larger strain rate corresponds to a smaller time interval for a given strain increment during each simulation step. When this time interval is significantly shorter than the average residence time, the probability of thermal plasticity occurring within the interval diminishes, delaying yielding and resulting in a higher yield strength. It's worth noting that at low strain rates, the yield stress increases linearly with strain rate, but at very high strain rates with reduced ductility, the increment in yield stress becomes smaller. This trend aligns with the experimental findings [48,50–52]. The saturation observed at extremely high strain rates occurs because the time interval becomes small enough compared to the average residence time, exerting no further influence in reducing the probability of yielding. Moreover, as evident in the analysis of extreme site occurrence and strain localization index (Fig. 7(d)), both increase as the strain rate escalates, indicating that higher strain rates are associated with reduced ductility. This effect arises from the autocatalytic effect introduced by softening. Analogous to the influence of the extent of AEBS shift during deformation (softening behavior) discussed in Section 3.2.1, higher strain rates lead to more pronounced shifts and greater softening effects, thereby impairing ductility.

Another crucial factor worth highlighting is temperature. According to Eq. (5), an elevation in temperature results in an increased activation rate, which yields a similar effect to the decrease in activation energy barrier. Consequently, at lower temperatures, the yield strength becomes exceedingly high while ductility significantly diminishes. Under such conditions, the probability of thermal plasticity occurring is already quite low, especially at small strain rates during which the temperature increase is insignificant. As a result, the yield strength exhibits minimal variation at lower strain rates, which is consistent with observations in numerous experiments [49–51,53]. Furthermore, it's essential to recognize that local temperatures increase during deformation. Empirical evidence [51,53] indicates that higher strain rates contribute to elevated local temperatures, which provides a similar effect as softening.

4.3. Limitations

In our current mesoscale simulations, we apply the homogeneous modulus assumption by assigning an identical elastic modulus to all voxels. The impact of the heterogeneity of shear modulus has been demonstrated in the work by Wang et al. [22]. Additionally, our model assumes that all STZs possess the same size as the voxel, which is different from what is suggested in atomistic simulations that the STZ size follows a distribution [16]. Nevertheless, atomistic simulation results do not clearly establish a direct correlation between STZ size and the AEBS. Hence, the uniform size assumption for STZs may have a limited effect on the AEBS and the associated outcomes. For simplicity, we exclusively consider the average and shift of the AEBS, presuming a uniform Gaussian width. This assumption draws from atomistic simulations, which suggest that the width of the AEBS remains nearly constant irrespective of cooling rate variations [19]. Furthermore, we only consider one type of STZ in the current study with the change of average activation energy barrier. In reality, structural heterogeneity in MGs is most likely to lead to different activation energy barriers and softening behaviors at different locations. Even though our atomistic simulations suggest that there only exist weak propensities rather than strong correlations between the local structural motifs (short-range orderings) and their activation barriers (shown in the Appendix), structural heterogeneities with medium-range ordering have been found and believed to play a key role in determining the deformation behavior of BMGs [2]. However, there is little information from atomistic simulations. The degree of such structural heterogeneity determines spatial variation of local activation energy barrier and softening behavior and, thus, the degree of autocatalysis, strain localization, and the mechanical properties of BMGs. The correlation between the structural heterogeneity and the properties of BMGs remains unclear. Consequently, further research is needed by directly incorporating quantitative experimental measurements and atomistic simulations of distinct types of STZs with heterogeneous structures, which deserve a separate study.

Our atomistically informed mesoscale model could be placed on a firmer (more self-consistent) footing if we make a direct comparison of the atomistic and mesoscale simulations at the same length and time scales before we integrate them together. Some attempts have been made to calibrate mesoscale models directly against atomistic simulation results. For example, Castellanos et al. [59,60] established a mesoscale elasto-plastic model by considering statistically distributed structural properties and elastic coupling between discrete blocks. They calibrated the model by matching the mechanical properties of the system to those obtained in the atomistic simulations at the same length scale. Since the main focus of the current study is to use the critical information about STZ activation derived from the atomistic simulations in our mesoscale modelling to capture the collective behavior of a large population of STZ events including autocatalysis that leads to strain localization, strain avalanche and formation of shear bands, such a one-on-one calibration between the atomistic and mesoscale simulations at the atomic scale is not made.

5. Summary

In the current study, we link the heterogeneously randomized shear transformation zone (STZ) model with a kinetic Monte Carlo algorithm directly to atomistic simulations, by extracting all the key parameters of STZs, including the number of shear modes, STZ size, eigenstrain, and the activation energy barrier spectrum (AEBS), directly from atomistic simulation results. This has allowed us to place the mesoscale modeling on a much rigorous and more firm theoretical footing. By considering two important parameters of the STZ AEBS (assumed following a Gaussian distribution): the average of the Gaussian distribution (determined by preparation history such as cooling rate of the MGs) and the amount of shift of the Gaussian distribution during deformation (the softening behavior), we simulate the deformation microstructure, shear band formation and the stress-strain behavior of BMGs, and demonstrate the effects of cooling rate and strain rate on the deformation behavior and mechanical properties of BMGs. The atomistically informed mesoscale simulation results reveal that the average of AEBS is responsible for the yield strength, while the amount of shift of AEBS during deformation (the softening behavior) is responsible for the ductility. These simulation results allow us to gain important insights about the effects of cooling rate and strain rate by linking their effects on the changes in AEBS, i.e., the lower is the cooling rate during glass preparation, the higher is the average of AEBS and the larger is the shift of AEBS (i.e., the larger is the degree of softening) and, thus, the higher is the yield strength and the lower is the ductility. On the other hand, the higher is the strain rate during deformation, the larger is the AEBS shift and, thus, the lower is the ductility.

CRediT authorship contribution statement

Yuchi Wang: Writing – review & editing, Writing – original draft, Visualization, Validation, Software, Methodology, Investigation, Formal analysis, Data curation, Conceptualization. **Yuchu Wang:** Visualization, Validation, Software, Methodology, Investigation, Formal analysis, Data curation. **Chaoyi Liu:** Software, Methodology, Data curation. **Jinwoo Hwang:** Writing – review & editing, Resources, Supervision, Project administration, Funding acquisition, Conceptualization. **Yue Fan:**

Writing – review & editing, Supervision, Resources, Project administration, Funding acquisition, Conceptualization. **Yunzhi Wang:** Writing – review & editing, Supervision, Resources, Project administration, Funding acquisition, Conceptualization.

Declaration of competing interests

The authors declare that they have no known competing financial interests or personal relationships that could have appeared to influence the work reported in this paper.

Acknowledgement

The authors acknowledge support from the National Science Foundation under grant NSF-DMR-2104724 and grant NSF-DMR-2104136.

Appendix

1. Validate the randomized eigenstrain directions for different shear modes

The distribution of the deformation events in strain space is assumed to be isotropic in the previous studies [29,30]. While some ART works [74–76] demonstrated that there are some quite different structural changes which show more string-like motions, we conduct atomistic simulations to scrutinize the displacement vectors (e.g. random vs. string-like) of the ART-probed local structural excitations at different global strain conditions. More specifically, adopting a protocol outlined in [77], we analyze atoms' displacement vectors between the initial and final states for each ART event. Note that only the atoms with relatively significant displacements (greater than 0.1 Å) are analyzed. The number of those significant atoms is denoted as N. Among these N atoms, we examine all possible pairs of atoms *i* and *j*. If the angle between displacement vectors $\vec{r}_i$ and $\vec{r}_j$ is less than 45°, then such a pair is labelled as "aligned". Mathematically, for a set of completely random directional vectors, the probability of finding an aligned pair of vectors within 45° should be $\left(1-\frac{\sqrt{2}}{2}\right)\approx 0.3$. Therefore, a string-like event should correspond to a higher fraction (>0.3) of "aligned" pairs out of the total N(N-1)/2 pairs, while a random event should correspond to a lower fraction around 0.3.

In Fig. A1 below we plot the histograms on the fractions of the aligned pairs under the global strain conditions of 0 % and 15 %, respectively. While indeed the strained sample shows some signatures of higher fraction of aligned pairs (i.e. more string-like events), the overall differences between the two histograms are small. And the vast majority of the events in both samples have the fraction around 0.3, indicating a nature of more random displacement fields. In other words, the assumption made in our mesoscale modeling, namely a randomly directional eigenstrains, should be valid.

2. The relationship between various structural motifs and their activation energies

To confirm how the structural heterogeneity could influence the activation energy barriers, we conduct analysis to probe the relationship between various local structural motifs and their activation energies. Here we use Voronoi index to characterize the local structural motifs, and we regard $\langle 0,0,12,0\rangle$ as the most stable motif while regard the indices with $2n_4+n_5\neq 12$ as the least stable motifs (following the protocol in [78]). In Fig. A2 below we show activation energy barriers spectra for the most stable (blue bars) and least stable (red bars) motifs, as well as their relative positions within the overall activation energy barriers spectrum (grey bars). Note that the overall spectrum also includes other motifs, such as the ones satisfying $2n_4+n_5=12$ but not $\langle 0,0,12,0\rangle$. It can be seen that there exists discernible difference between the blue and red spectra, and indeed the $\langle 0,0,12,0\rangle$ motifs yield statistically high activation barriers. That said, the two spectra of different motifs exhibit very broad distributions and still significantly overlap with each other. This suggests that there only exist weak propensities but not strong correlations between the local structural motifs and their activation barriers. Similar results were also reported in [79], where short-range ordering was found to have certain correlation with the location of plastic events, but it is too weak to make a difference.

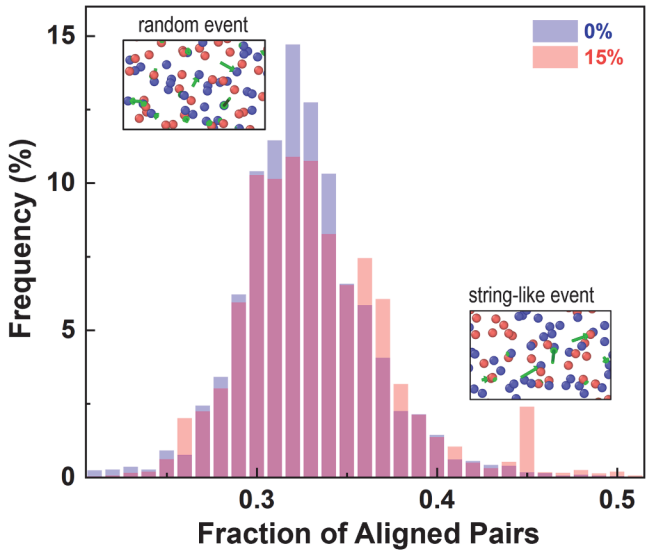

Fig. A1. Histograms comparison on the fraction of aligned pairs in 0 % and 15 % strained samples.

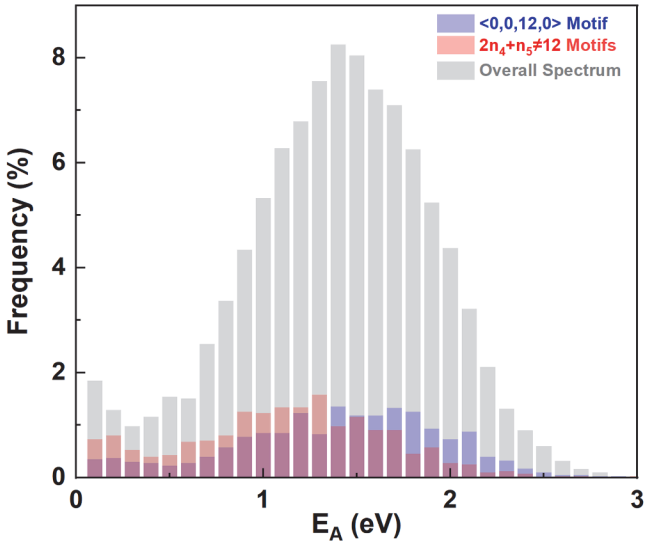

Fig. A2. Histograms of activation barriers spectra for the most and least stable motifs, as well as their relative positions within the overall spectrum.

References

[1] J.M. Park, J.H. Han, N. Mattern, D.H. Kim, J. Eckert, Designing Zr-Cu-Co-Al bulk metallic glasses with phase separation mediated plasticity, Metall. Mater. Trans. A 43 (2012) 2598–2603.

[2] S. Im, Y. Wang, P. Zhao, G.H. Yoo, Z. Chen, G. Calderon, M.A. Gharacheh, M. Zhu, O. Licata, B. Mazumder, D.A. Muller, E.S. Park, Y. Wang, J. Hwang, Medium-range ordering, structural heterogeneity, and their influence on properties of Zr-Cu-Co-Al metallic glasses, Phys. Rev. Mater. 5 (11) (2021) 115604.

[3] Y.H. Liu, G. Wang, R.J. Wang, D.Q. Zhao, M.X. Pan, W.H. Wang, Super plastic bulk metallic glasses at room temperature, Science (1979) 315 (5817) (2007) 1385–1388.

[4] B. Zhang, D.Q. Zhao, M.X. Pan, W.H. Wang, A.L. Greer, Amorphous metallic plastic, Phys. Rev. Lett. 94 (2005) 205502.

[5] S. Takeuchi, K. Edagawa, Atomistic simulation and modeling of localized shear deformation in metallic glasses, Prog. Mater. Sci. 56 (6) (2011) 785–816.

[6] M.L. Falk, J.S. Langer, Dynamics of viscoplastic deformation in amorphous solids, Phys. Rev. E 57 (6) (1998) 7192.

[7] F. Shimizu, S. Ogata, J. Li, Yield point of metallic glass, Acta Mater. 54 (16) (2006) 4293–4298.

[8] F. Shimizu, S. Ogata, J. Li, Theory of shear banding in metallic glasses and molecular dynamics calculations, Mater. Trans. 48 (11) (2007) 2923–2927.

[9] S. Hara, J. Li, Adaptive strain-boost hyperdynamics simulations of stress-driven atomic processes, Phys. Rev. B 82 (18) (2010) 184114.

[10] M.L. Manning, A.J. Liu, Vibrational modes identify soft spots in a sheared disordered packing, Phys. Rev. Lett. 107 (10) (2011) 108302.

[11] J. Ding, S. Patinet, M.L. Falk, Y. Cheng, E. Ma, Soft spots and their structural signature in a metallic glass, Proc. Natl. Acad. Sci. 111 (39) (2014) 14052–14056.

[12] Z.Y. Yang, L.H. Dai, Towards commonality between shear banding and glass-liquid transition in metallic glasses, Phys. Rev. Mater. 6 (10) (2022) L100602.

[13] A.J. Cao, Y.Q. Cheng, E. Ma, Structural processes that initiate shear localization in metallic glass, Acta Mater. 57 (17) (2009) 5146–5155.

[14] S. Feng, L. Qi, L. Wang, S. Pan, M. Ma, X. Zhang, G. Li, R. Liu, Atomic structure of shear bands in Cu64Zr36 metallic glasses studied by molecular dynamics simulations, Acta Mater. 95 (2015) 236–243.

[15] Y. Fan, T. Iwashita, T. Egami, Evolution of elastic heterogeneity during aging in metallic glasses, Phys. Rev. E 89 (6) (2014) 062313.

[16] Y. Fan, T. Iwashita, T. Egami, How thermally activated deformation starts in metallic glass, Nat. Commun. 5 (1) (2014) 5083.

[17] D. Rodney, C. Schuh, Distribution of thermally activated plastic events in a flowing glass, Phys. Rev. Lett. 102 (23) (2009) 235503.

[18] Y. Fan, T. Iwashita, T. Egami, Crossover from localized to cascade relaxations in metallic glasses, Phys. Rev. Lett. 115 (4) (2015) 045501.

[19] Y. Fan, T. Iwashita, T. Egami, Energy landscape-driven non-equilibrium evolution of inherent structure in disordered material, Nat. Commun. 8 (1) (2017) 15417.

[20] C. Liu, P. Guan, Y. Fan, Correlating defects density in metallic glasses with the distribution of inherent structures in potential energy landscape, Acta Mater. 161 (2018) 295–301.

[21] C. Liu, Y. Fan, Emergent fractal energy landscape as the origin of stress-accelerated dynamics in amorphous solids, Phys. Rev. Lett. 127 (21) (2021) 215502.

[22] N. Wang, J. Ding, F. Yan, M. Asta, R.O. Ritchie, L. Li, Spatial correlation of elastic heterogeneity tunes the deformation behavior of metallic glasses, Npj Comput. Mater. 4 (2018) 19.

[23] D.J. Lacks, M.J. Osborne, Energy landscape picture of overaging and rejuvenation in a sheared glass, Phys. Rev. Lett. 93 (25) (2004) 255501.

[24] F.H. Stillinger, A topographic view of supercooled liquids and glass formation, Science (1979) 267 (5206) (1995) 1935–1939.

[25] P.G. Debenedetti, F.H. Stillinger, Supercooled liquids and the glass transition, Nature 410 (6825) (2001) 259–267.

[26] A.S. Argon, Plastic deformation in metallic glasses, Acta metallurgica 27 (1) (1979) 47–58.

[27] V.V. Bulatov, A.S. Argon, A stochastic model for continuum elasto-plastic behavior. I. Numerical approach and strain localization. Modelling and Simulation in, Mater. Sci. Eng. 2 (2) (1994) 167.

[28] E.R. Homer, C.A. Schuh, Mesoscale modeling of amorphous metals by shear transformation zone dynamics, Acta Mater. 57 (9) (2009) 2823–2833.

[29] P. Zhao, J. Li, Y. Wang, Heterogeneously randomized STZ model of metallic glasses: softening and extreme value statistics during deformation, Int. J. Plast. 40 (2013) 1–22.

[30] P. Zhao, J. Li, J. Hwang, Y. Wang, Influence of nanoscale structural heterogeneity on shear banding in metallic glasses, Acta Mater. 134 (2017) 104–115.

[31] G.T. Barkema, N. Mousseau, Event-based relaxation of continuous disordered systems, Phys. Rev. Lett. 77 (21) (1996) 4358.

[32] N. Mousseau, G.T. Barkema, Traveling through potential energy landscapes of disordered materials: the activation-relaxation technique, Phys. Rev. E 57 (2) (1998) 2419.

[33] E. Cances, F. Legoll, M.C. Marinica, K. Minoukadeh, F. Willaime, Some improvements of the activation-relaxation technique method for finding transition pathways on potential energy surfaces, J. Chem. Phys. 130 (2009) 114711.

[34] H. Kallel, N. Mousseau, F. Schiettekatte, Evolution of the potential-energy surface of amorphous silicon, Phys. Rev. Lett. 105 (4) (2010) 045503.

[35] C. Liu, X. Yan, P. Sharma, Y. Fan, Unraveling the non-monotonic ageing of metallic glasses in the metastability-temperature space, Comput. Mater. Sci. 172 (2020) 109347.

[36] V.K. Sethi, R. Gibala, A.H. Heuer, Transmission electron microscopy of shear bands in amorphous metallic alloys, Scripta Metallurgica 12 (2) (1978) 207–209.

[37] P.E. Donovan, W.M. Stobbs, The structure of shear bands in metallic glasses, Acta Metallurgica 29 (8) (1981) 1419–1436.

[38] J. Li, F. Spaepen, T.C. Hufnagel, Nanometre-scale defects in shear bands in a metallic glass, Philos. Mag. A 82 (13) (2002) 2623–2630.

[39] Z.W. Shan, J. Li, Y.Q. Cheng, A.M. Minor, S.S. Asif, O.L. Warren, E. Ma, Plastic flow and failure resistance of metallic glass: insight from in situ compression of nanopillars, Phys. Rev. B 77 (15) (2008).

[40] A.S. Argon, Strain avalanches in plasticity, Philos. Mag. 93 (28–30) (2013) 3795–3808.

[41] L. Li, E.R. Homer, C.A. Schuh, Shear transformation zone dynamics model for metallic glasses incorporating free volume as a state variable, Acta Mater. 61 (9) (2013) 3347–3359.

[42] L. Li, N. Wang, F. Yan, Transient response in metallic glass deformation: a study based on shear transformation zone dynamics simulations, Scr. Mater. 80 (2014) 25–28.

[43] A. Dubach, F.H. Dalla Torre, J.F. Löffler, Deformation kinetics in Zr-based bulk metallic glasses and its dependence on temperature and strain-rate sensitivity, Philos. Mag. Lett. 87 (9) (2007) 695–704.

[44] Y.J. Huang, J. Shen, J.F. Sun, Bulk metallic glasses: smaller is softer, Appl. Phys. Lett. 90 (8) (2007).

[45] Y. Liu, H. Bei, C.T. Liu, E.P. George, Cooling-rate induced softening in a $Zr_{50}Cu_{50}$ bulk metallic glass, Appl. Phys. Lett. 90 (7) (2007).
[46] D. Singh, R.K. Mandal, R.S. Tiwari, O.N. Srivastava, Effect of cooling rate on the crystallization and mechanical behaviour of Zr–Ga–Cu–Ni metallic glass composition, J. Alloys Compd. 648 (2015) 456–462.
[47] Z.Y. Liu, Y. Yang, S. Guo, X.J. Liu, J. Lu, Y.H. Liu, C.T. Liu, Cooling rate effect on Young's modulus and hardness of a Zr-based metallic glass, J. Alloys Compd. 509 (7) (2011) 3269–3273.
[48] C.A. Schuh, T.C. Hufnagel, U. Ramamurty, Mechanical behavior of amorphous alloys, Acta Mater. 55 (12) (2007) 4067–4109.
[49] T. Mukai, T.G. Nieh, Y. Kawamura, A. Inoue, K. Higashi, Effect of strain rate on compressive behavior of a $Pd_{40}Ni_{40}P_{20}$ bulk metallic glass, Intermetallics. (Barking) 10 (11–12) (2002) 1071–1077.
[50] J. Lu, G. Ravichandran, W.L. Johnson, Deformation behavior of the $Zr_{41.2}Ti_{13.8}Cu_{12.5}Ni_{10}Be_{22.5}$ bulk metallic glass over a wide range of strain-rates and temperatures, Acta Mater. 51 (12) (2003) 3429–3443.
[51] J. Zhang, J.M. Park, D.H. Kim, H.S. Kim, Effect of strain rate on compressive behavior of $Ti_{45}Zr_{16}Ni_9Cu_{10}Be_{20}$ bulk metallic glass, Mater. Sci. Eng. 449 (2007) 290–294.
[52] P.S. Singh, R.L. Narayan, I. Sen, D.C. Hofmann, U. Ramamurty, Effect of strain rate and temperature on the plastic deformation behaviour of a bulk metallic glass composite, Mater. Sci. Eng. 534 (2012) 476–484.
[53] M.C. Li, M.Q. Jiang, S. Yang, F. Jiang, L. He, J. Sun, Effect of strain rate on yielding strength of a Zr-based bulk metallic glass, Mater. Sci. Eng. 680 (2017) 21–26.
[54] Y.Q. Cheng, E. Ma, H.W. Sheng, Atomic level structure in multicomponent bulk metallic glass, Phys. Rev. Lett. 102 (24) (2009) 245501.
[55] P. Guan, M. Chen, T. Egami, Stress-temperature scaling for steady-state flow in metallic glasses, Phys. Rev. Lett. 104 (20) (2010) 205701.
[56] J. Ding, Y.Q. Cheng, E. Ma, Full icosahedra dominate local order in $Cu_{64}Zr_{34}$ metallic glass and supercooled liquid, Acta Mater. 69 (2014) 343–354.
[57] Y. Wu, D. Ma, Q.K. Li, A.D. Stoica, W.L. Song, H. Wang, X.J. Liu, G.M. Stoica, G. Y. Wang, K. An, X.L. Wang, Mo Li, Z.P. Lu, Transformation-induced plasticity in bulk metallic glass composites evidenced by in-situ neutron diffraction, Acta Mater. 124 (2017) 478–488.
[58] Z. Fan, E. Ma, Predicting orientation-dependent plastic susceptibility from static structure in amorphous solids via deep learning, Nat. Commun. 12 (1) (2021) 1506.
[59] D.F. Castellanos, S. Roux, S. Patinet, Insights from the quantitative calibration of an elasto-plastic model from a Lennard-Jones atomic glass, C. R. Phys. 22 (S3) (2021) 1–28.
[60] D.F. Castellanos, S. Roux, S. Patinet, History dependent plasticity of glass: a mapping between atomistic and elasto-plastic models, Acta Mater. 241 (2022) 118405.
[61] J.S. Langer, Dynamics of shear-transformation zones in amorphous plasticity: formulation in terms of an effective disorder temperature, Phys. Rev. E 70 (4) (2004) 041502.
[62] Y. Shi, M.B. Katz, H. Li, M.L. Falk, Evaluation of the disorder temperature and free-volume formalisms via simulations of shear banding in amorphous solids, Phys. Rev. Lett. 98 (18) (2007) 185505.
[63] M.J. Kramer, H. Mecco, K.W. Dennis, E. Vargonova, R.W. McCallum, R. E. Napolitano, Rapid solidification and metallic glass formation–Experimental and theoretical limits, J. Non Cryst. Solids 353 (32–40) (2007) 3633–3639.
[64] J.D. Eshelby, The determination of the elastic field of an ellipsoidal inclusion, and related problems, Proc. R. Soc. Lond. Ser. A. Math. Phys. Sci. 241 (1226) (1957) 376–396.
[65] A. Voter, Introduction to the kinetic Monte Carlo method, in: K. Sickafus, E. Kotomin, B. Uberuaga (Eds.), Radiation Effects in Solids, Springer, 2007.
[66] X.K. Xi, D.Q. Zhao, M.X. Pan, W.H. Wang, Y. Wu, J.J. Lewandowski, Fracture of brittle metallic glasses: brittleness or plasticity, Phys. Rev. Lett. 94 (12) (2005) 125510.
[67] H. Bei, S. Xie, E.P. George, Softening caused by profuse shear banding in a bulk metallic glass, Phys. Rev. Lett. 96 (10) (2006) 105503.
[68] F. Spaepen, A microscopic mechanism for steady state inhomogeneous flow in metallic glasses, Acta metallurgica 25 (4) (1977) 407–415.
[69] D. Rodney, T. Schrøder, On the potential energy landscape of supercooled liquids and glasses, Eur. Phys. J. E 34 (2011) 1–7.
[70] D. Rodney, A. Tanguy, D. Vandembroucq, Modeling the mechanics of amorphous solids at different length scale and time scale, Model. Simul. Mat. Sci. Eng. 19 (8) (2011) 083001.
[71] P. Koziatek, J.L. Barrat, P. Derlet, D. Rodney, Inverse Meyer-Neldel behavior for activated processes in model glasses, Phys. Rev. B 87 (22) (2013) 224105.
[72] A. Barbot, M. Lerbinger, A. Lemaitre, D. Vandembroucq, S. Patinet, Rejuvenation and shear banding in model amorphous solids, Phys. Rev. E 101 (3) (2020) 033001.
[73] M. Popović, T.W. de Geus, M. Wyart, Elastoplastic description of sudden failure in athermal amorphous materials during quasistatic loading, Phys. Rev. E 98 (4) (2018) 040901.
[74] S. Swayamjyoti, J.F. Löffler, P.M. Derlet, Local structural excitations in model glasses, Phys. Rev. B 89 (22) (2014) 224201.
[75] S. Swayamjyoti, J.F. Löffler, P.M. Derlet, Local structural excitations in model glass systems under applied load, Phys. Rev. B 93 (14) (2016) 144202.
[76] S. Swayamjyoti, J.F. Löffler, P.M. Derlet, Erratum: local structural excitations in model glass systems under applied load [Phys. Rev. B 93, 144202 (2016)], Phys. Rev. B 98 (21) (2018) 219904.
[77] X.T. Li, X.Z. Tang, Y.F. Guo, H. Li, Y. Fan, Modulating grain boundary-mediated plasticity of high-entropy alloys via chemo-mechanical coupling, Acta Mater. 258 (2023) 119228.
[78] C. Liu, Y. Wang, Y. Wang, M. Islam, J. Hwang, Y. Wang, Y. Fan, Concurrent prediction of metallic glasses' global energy and internal structural heterogeneity by interpretable machine learning, Acta Mater. 259 (2023) 119281.
[79] S. Patinet, D. Vandembroucq, M.L. Falk, Connecting local yield stresses with plastic activity in amorphous solids, Phys. Rev. Lett. 117 (4) (2016) 045501.